Multi-plane spatially resolved phase structuring using optical communication modes

Journal of Optics

OPEN ACCESS

RECEIVED
14 March 2026

REVISED
7 May 2026

ACCEPTED FOR PUBLICATION
20 May 2026

PUBLISHED
8 June 2026

PAPER

Multi-plane spatially resolved phase structuring using optical communication modes

Vinicius S de Angelis[1,4,*], **Maximilian Jeindl**[2], **Leonardo A Ambrosio**[1], **David A B Miller**[3], **Federico Capasso**[4] and **Ahmed H Dorrah**[2,4,*]

[1] Department of Electrical and Computer Engineering, São Carlos School of Engineering, University of São Paulo, 400 Trabalhador São-Carlense Ave., 13566-590 São Carlos, São Paulo, Brazil
[2] Department of Applied Physics and Science Education, Eindhoven University of Technology, Eindhoven 5612 AP, The Netherlands
[3] Ginzton Laboratory, Stanford University, Stanford, CA 94305, United States of America
[4] Harvard John A. Paulson School of Engineering and Applied Sciences, Harvard University, Cambridge, MA 02138, United States of America
[*] Authors to whom any correspondence should be addressed.

E-mail: vinicius.angelis@usp.br and a.h.dorrah@tue.nl

Keywords: structured light, wavefront shaping, optical communication modes, multi-plane holography, phase structuring, optical phase singularities

Supplementary material for this article is available online

Abstract

We present a deterministic framework for three-dimensional beam shaping that enables versatile control of intensity and phase, pixel-by-pixel, across multiple axial planes. Conventional multi-plane holographic techniques typically rely on iterative optimization and mitigate inter-plane crosstalk through phase randomization, introducing speckle noise and thereby limiting deterministic phase control. Here, target fields are synthesized as a linear superposition of free-space communication modes obtained from the singular value decomposition of a coupling operator connecting a source plane to multiple target planes. Because these modes form orthogonal and energy-efficient transmission channels between the source and receiving spaces, their superposition yields volumetric wavefields with enforced phase coherence and reduced inter-plane crosstalk, without iterative refinement. We experimentally demonstrate high-fidelity reconstruction of intensity and phase profiles across multiple planes using a single phase-only spatial light modulator, including arbitrary structured phase singularity patterns. The proposed approach establishes communication-mode optics as a practical and physically grounded framework for multi-plane beam shaping, particularly in applications where phase structure and coherence across depth are essential.

1. Introduction

Three-dimensional (3D) control of optical wavefields underpins applications in holography, optical manipulation, volumetric imaging, and diffractive optical systems [1–6]. While considerable progress has been made in synthesizing prescribed intensity distributions across multiple axial planes, deterministic control of phase distributions remains an outstanding challenge. Most multi-plane holographic techniques rely on iterative wave-propagation algorithms [7–10], such as Global Gerchberg–Saxton (GGS) methods [11, 12] or stochastic gradient descent (SGD) optimization schemes [13, 14], to compute a single phase mask that reproduces target patterns at multiple depths. In these approaches, inter-plane crosstalk arises from the unavoidable overlap of reconstructed fields at adjacent planes, leading to ghost images and loss of contrast. Crosstalk suppression is commonly achieved by intentionally de-correlating the target planes, most notably by imposing random phase distributions [15]. While random-phase encoding effectively suppresses coherent leakage between planes, it fundamentally precludes deterministic

phase control and inevitably introduces speckle noise [16, 17]. Even advanced algorithms that explicitly penalize crosstalk and impose phase regularization, such as compensatory GGS [18] and double-constraint SGD methods [19], remain incapable of eliminating all speckles—an inherent limitation rooted in the phenomenon of vortex stagnation [20]. As a result, existing multi-plane holographic techniques typically sacrifice phase determinism in exchange for intensity fidelity. This limitation is fundamental; namely, intensity-only multi-plane holography using a static computer-generated hologram (CGH) under coherent illumination produces layered images rather than a single physically consistent wavefront.

On the other hand, phase consistency across axial planes is desirable as it ensures that the reconstructed fields correspond to a single physically valid wavefront, thereby preserving correct wavefront curvature and enabling genuine 3D depth cues [21]. Beyond imaging, multi-plane phase control is also essential for compensating depth-dependent aberrations [22, 23], thereby enabling volumetric adaptive optics rather than a single global correction. Furthermore, the ability to control the phase profile at each plane allows the engineering of topological wavefields across planes, including phase singularities [24–26] that give rise to stacked on-demand blue-detuned optical trap arrays (for atom trapping) and genuinely volumetric trapping architectures, rather than isolated single-point traps [27–29] or single-plane traps [30–32]. Finally, tailoring phase gradients enables the design of 3D optical force landscapes that support controlled rotation and circulation of particles, extending beyond the static trapping afforded by intensity gradients alone [33, 34]. Nevertheless, a systematic framework that allows the phase profile to be arbitrarily structured, point-by-point, along the optical path remains elusive.

In this work, we propose and demonstrate a versatile method for controlling intensity and phase across multiple planes. The target field distributions are synthesized from a linear superposition of the communication modes connecting a source plane to the set of target planes. These modes are obtained using the singular value decomposition (SVD) modal optics [35]. We encode the radiative near-field (Fresnel region) from the required source distribution into a CGH phase mask and optically reconstruct the resulting wavefront using a phase-only spatial light modulator (SLM). While communication mode theory [36] originally established the foundations of SVD modal analysis, prior studies considered only theoretical scenarios in simplified geometries using prolate spheroidal functions [37–39]. A practical and experimentally validated framework for volumetric wavefront shaping with continuous depth of field has only recently been demonstrated [40]. Here, we expand on this direction by focusing on multi-plane beam shaping and demonstrating on-demand, spatially-resolved, phase control.

Because the communication modes represent the optimal orthogonal channels connecting the source and receiving spaces [35], the computed source distribution is expected to produce reconstructed intensity profiles with minimal crosstalk, high contrast and fidelity due to the efficient energy transfer of the modes among the target planes. Although iterative hologram synthesis can suppress speckle noise by initializing the target planes with well-defined phase distributions, notably constant and quadratic phase initializations [17, 41–43], the choice of phase initialization influences both the convergence behavior and the achievable reconstruction accuracy, potentially converging to sub-optimal solutions, as the synthesis constitutes a non-convex optimization problem [44]. Our method, by contrast, is deterministic and requires no iterative refinement or inverse-design procedures. Moreover, since the communication modes are continuous complex-valued eigenfunctions, our method not only yields speckle-free intensity reconstructions but also enables the structuring of arbitrary phase distributions with high fidelity. To our knowledge, this work represents the first adaptation of SVD modal optics as a general and experimentally validated framework for multi-plane beam shaping of arbitrary complex-valued fields.

2. Concept

Each communication mode comprises a pair of eigenfunctions: one defined at the source space that leads to another at the receiving space. For scalar waves in free space, these eigenfunctions are connected to each other by a coupling operator G_{SR} described by a scalar Green's function. Modeling the spaces as being composed of sufficiently dense arrays of N_S source and N_R receiving points, G_{SR} is expressed by a $N_S \times N_R$ matrix with its singular values s_j establishing the connection between each pair of source $|\Psi_{S,j}\rangle$ and receiving $|\Phi_{R,j}\rangle$ eigenfunctions (standard Dirac 'bra-ket' notation is used). In particular, these eigenfunctions satisfy the relationship $G_{SR}|\Psi_{S,j}\rangle = s_j|\Phi_{R,j}\rangle$, with $|s_j|^2$ quantifying their coupling strength. See Methods and [35] for a detailed description of the communication mode theory.

For our multi-plane application, first we consider a source plane with transverse dimensions $X_s = Y_s$ and located at $z = 0$, as depicted in figure 1(a). The receiving space consists of a set of n transverse planes, uniformly spaced and without lateral shift; the distance from the source aperture to the nth plane

Table 1. Parameters adopted for the source and receiving spaces of figure 1(a). Number of source and receiving points, spacing distances and longitudinal separation distance L_0 between the spaces.

Source plane			Receiving space	
$p_x \times p_y$	d_x,d_y	L_0	array of points	spacing distances
251×251	4λ	4000λ	$p_{x,r} \times p_{y,r} = 21 \times 21$	$d_{x,n} = d_{y,n} = 2\lambda[1 + (n-1)(L/L_0)]$

is $z_n = L_0 + (n-1)L$, where L_0 is the separation distance between the spaces. To remain in the paraxial regime we set $L_0 = 4Y_s$. Each receiving plane is sampled by an array of $p_{x,r} \times p_{y,r}$ receiving points, while the source plane is composed of $p_x \times p_y$ source points. We design the receiving planes such that all of them support the same number N of strongly coupled modes. To achieve this, all planes subtend the same solid angle from the source aperture, which requires the spacing distances $d_{x,n} = d_{y,n}$ between receiving points to increase linearly from plane to plane. The number N of strongly coupled modes follows from the Nyquist sampling criterion applied to the minimum resolvable spot size at each receiving plane, and depends only on the size of the receiving array (see equation (8)). Finally, the spacing between source points, $d_x = d_y$, is chosen to ensure that the wavefront created by the discrete set of N_S source points converges to that of a continuous source distribution (see methods).

Table 1 lists the parameter values adopted for the configuration of figure 1(a). With the chosen array size for the receiving points ($p_{x,r} = p_{y,r} = 21$), each receiving plane supports a total number of $N = 100$ strongly coupled modes. For operation at $\lambda = 532$ nm, the coupling strengths $|s_j|^2$ in order of decreasing magnitude associated with these modes for $L = L_0$ are shown in figure 1(b) (black solid line). The range of strongly coupled modes of each plane is indicated in yellow. For comparison, we also plot the coupling strengths obtained when each receiving plane is considered individually in the absence of the other two. This is indicated by the red, blue, and green dotted points, respectively. The difference in the behavior of the coupling strengths between the individual and combined multi-plane scenarios—see encircled regions in figure 1(b) — reveals that the strongly coupled modes of each nth receiving plane can be classified into two subcategories: (i) modes inherent to the nth plane and independent of the other receiving planes; and (ii) modes that arise only in a multi-plane configuration. We refer to modes of the first category as intrinsic and to those of the second as extrinsic. The coupling strengths of the intrinsic modes remain nearly constant over their respective ranges and decay from plane to plane according to the same inverse-square falloff as the intensity from an on-axis source point (see supplementary note 1).

Although the number of intrinsic and extrinsic modes varies from plane to plane, their sum is constant: $N_{\text{int},n} + N_{\text{ext},n} = N$. In particular, $N_{\text{ext},1} = 3$ and $N_{\text{ext},2} = 16$, as depicted by the encircled regions in figure 1(b). Figures 1(c)–(h) show the normalized intensity distributions of selected modes at the source plane (left) and on the propagation horizontal xz plane (right). The first extrinsic ($j = 1$) and intrinsic ($j = 4$) modes are shown in figures 1(c) and (d) with the inset figures displaying the transverse intensity distribution at the first plane. In the xy plane, intrinsic modes exhibit spatially localized structures, focused at the corresponding receiving plane, whereas extrinsic modes tend to display smoother, more de-localized profiles, with energy flow extending beyond the corresponding plane. Additionally, both intrinsic and extrinsic modes maintain phase consistency across the receiving planes with no random phase perturbations as depicted in figures 1(i)–(j). The last strong mode ($j = 100$) associated with the first plane is shown in figure 1(e). Partially coupled modes between the strong modes of the first and second planes occupy the range $101 \leqslant j \leqslant 120$ — see mode $j = 101$ in figure 1(f). The source intensity distributions of these modes are concentrated at the edges of the source aperture. Figures 1(g)–(h) show the first extrinsic and intrinsic modes associated with the second plane ($N_{\text{ext},2} = 16$). Supplementary video 1 displays the distributions of all the first 400 modes, including the intensity and phase distributions at the three receiving planes.

Between the regions of strongly coupled modes, there exist partially coupled modes that are not captured by equation (8). Because of these intermediate modes, the coupling strength curve deviates from an ideal step function. The strongly coupled modes in the second and third planes begin at $j = 121$ and $j = 257$, respectively. Following the strong modes of the final plane ($j \geqslant 357$), the coupling strengths decrease sharply, as illustrated by the logarithmic inset in figure 1(b), marking the onset of weakly coupled modes. This rapid fall off is universal, demonstrated for any finite geometries for the source and receiving spaces and explained by the tunneling-escape behavior of waves [45]. As a result, the rapid singular value decay limits the number of usable modes (in this case $M = 357$) [46]. For a paraxial configuration with a single receiving plane, this number corresponds to the paraxial heuristic number of equation (7), which is consistent with the space–bandwidth product in Fourier optics [35].

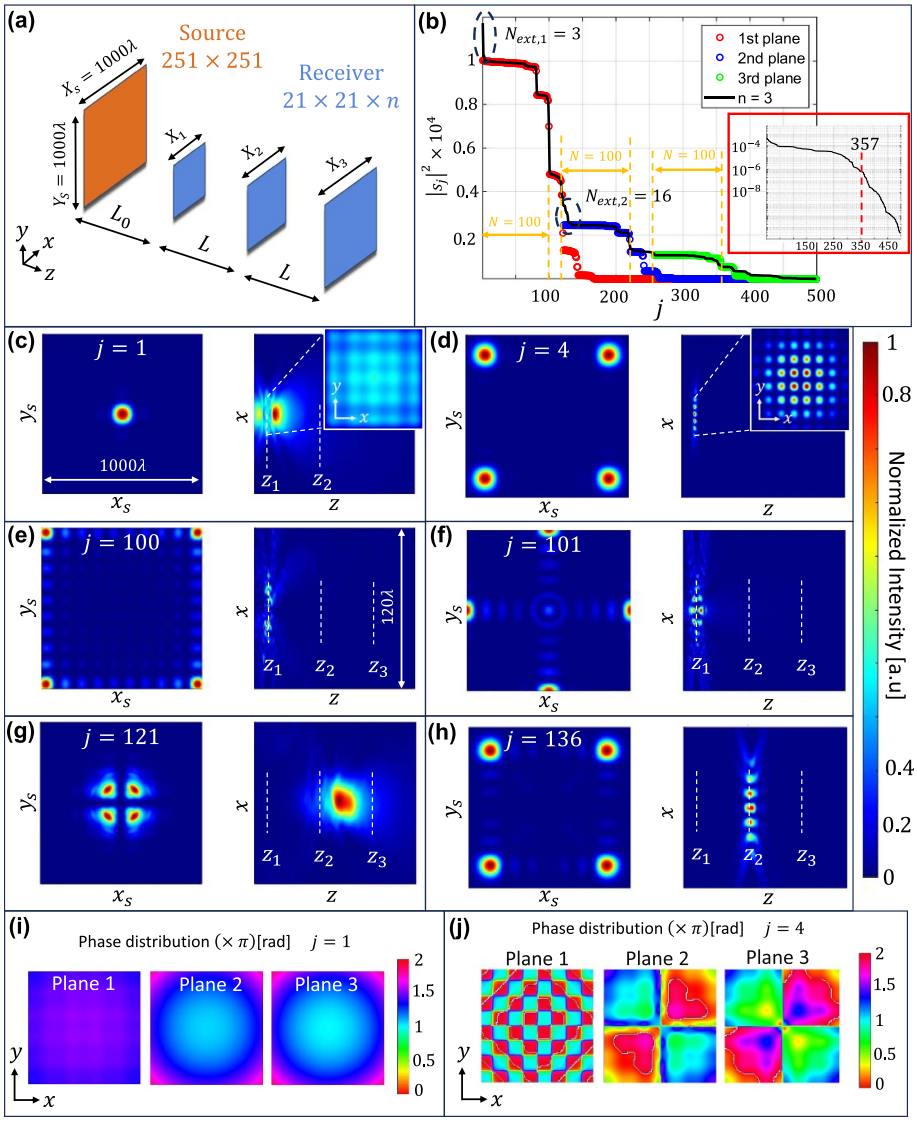

Figure 1. Communication modes and their coupling strengths associated with a transverse source plane and a set of three transverse receiving planes equally spaced from each other. (a) Dimensions of the source and receiving spaces, parametrized as listed in table 1 for $n = 3$ receiving planes. (b) Coupling strengths in order of decreasing magnitude computed at $\lambda = 532$ nm (black solid line). For comparison, the coupling strengths associated with each receiving plane separately are also shown (circle markers). Each nth receiving plane supports a total of $N = 100$ strongly coupled modes, and their range is indicated in yellow. Inset figure shows the coupling strengths on a log scale. These strong modes are classified into two sub-categories: intrinsic and extrinsic modes. Between the range of strong modes, there are also partially coupled modes. (c)–(h) Source eigenfunction intensity (on the left) and its resulting wave (on the right) along the xz plane for the modes: (c) $j = 1$ (extrinsic), (d) $j = 4$ and (e) $j = 100$ (intrinsic modes), (f) $j = 101$ (partially coupled mode), (g) $j = 121$ (extrinsic), (h) and $j = 136$ (intrinsic). For better visualization, these intensity distributions are normalized for each mode. (i)–(j) Transverse phase distributions across the receiving planes of the modes $j = 1$ and $j = 4$. Inset figures in (c) and (d) show the transverse intensity distribution at the first plane.

As the separation distance between the receiving planes decreases, the number of extrinsic strong modes increases. This is illustrated in figure 2(a), which shows the coupling strengths for different values of the ratio L/L_0 in the configuration of figure 1(a). Consequently, modes that originate from the whole receiving space become increasingly important for synthesizing light waves when the separation distances are reduced. However, upon further reduction of these distances, the total number of strongly coupled modes begins to decrease. This occurs for $L = 0.125L_0$, in which the number of strongly coupled modes in the second plane falls significantly below our design number of 100. As a result, the coupling strengths decay much more rapidly than for larger values of L/L_0 (see the inset of figure 2(a), which shows the coupling strengths on a logarithmic scale), thereby limiting the number of usable modes available for structuring arbitrary light-wave profiles.

We next synthesize arbitrary structured light profiles in the receiving planes. First, the target profile is represented as a vector of complex amplitudes Φ_T at the receiving points and we project that

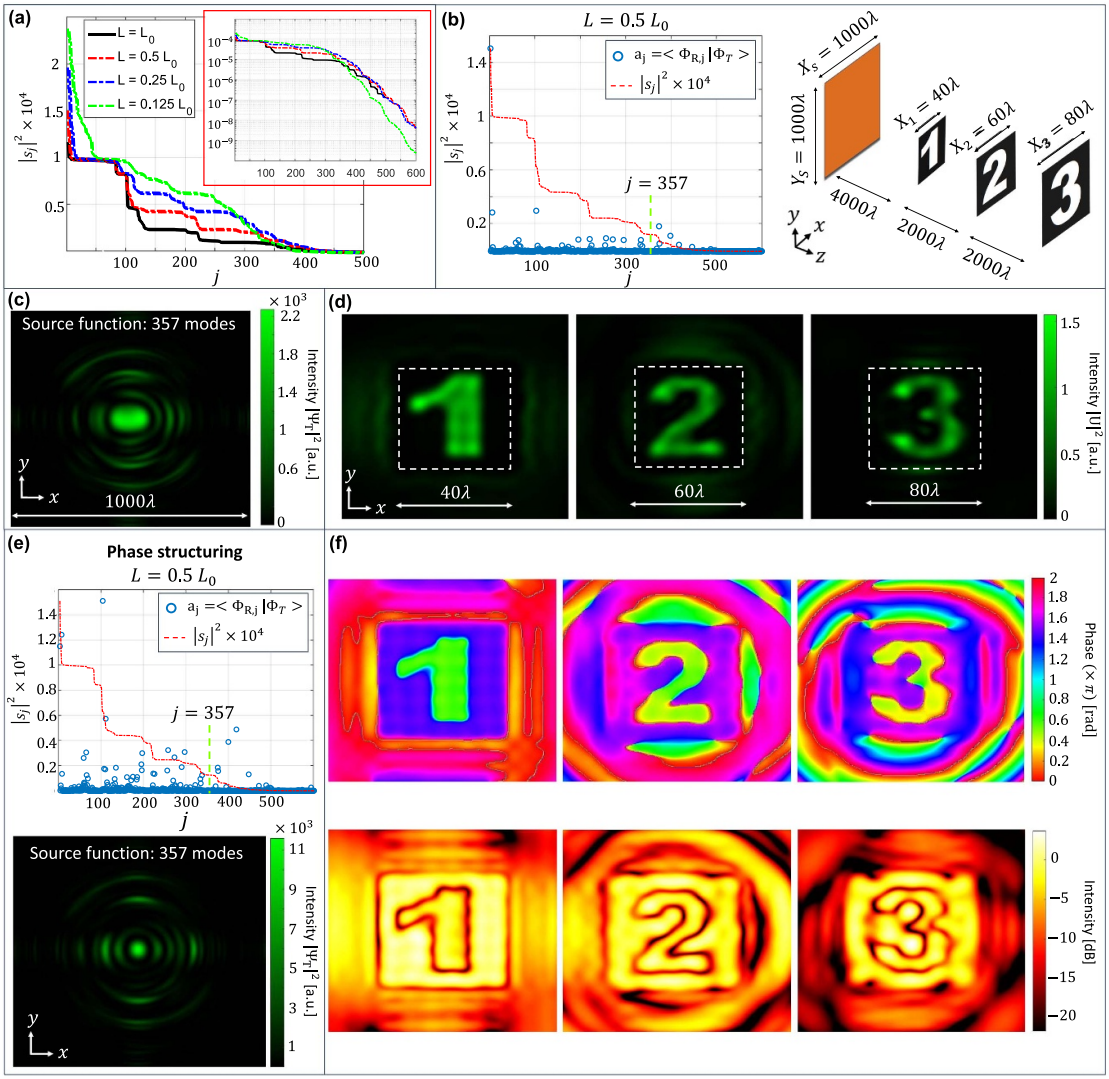

Figure 2. Simulated structuring of arbitrary light wave profiles. (a) Coupling strengths for different separation distances L between the receiving planes in the configuration of figure 1(a). The inset depicts the coupling strengths on a logarithmic scale. (b) For $L = 0.5L_0$, projection of a target intensity profile consisting of the binary digits '1', '2' and '3' onto the receiving basis set (blue circles). (c) Calculated source function computed from the first 357 well-coupled modes (strong and partially coupled modes). (d) Calculated resulting wave from the source function in all three receiving planes. The dashed white squares highlight the size of the target planes. (e) Structuring phase profiles: the target consists of the same three binary digits with a phase of $\pi/2$ radians inside each digit's contour and $3\pi/2$ radians outside. Amplitude is set to zero along each singularity contour (see figure S5). Projection onto the receiving basis set (blue circles) and calculated source function computed from the first 357 well-coupled modes (bottom). (f) Calculated phase and intensity (in dB) of the resulting wave in all three receiving planes.

profile onto the receiving basis. Finally, the required source function is computed as a linear superposition of the source components that create each receiving contribution of the target profile, akin to a Fourier series (see Methods). As an example, we consider as a target profile the intensity of digits '1,'2', and '3', assigned to each of the three receiving planes of the configuration of figure 1 for $L = 0.5L_0$—see figure 2(b). The inner product coefficients between the receiving eigenfunctions and this target profile are shown in figure 2(b), depicted by the blue circles. For reference, the coupling strengths $|s_j|^2$ of this distribution are also shown by the red dashed line. Using equations (11) and (12), we compute the required source function (figure 2(c) shows the squared amplitude) using the first 357 well-coupled modes (strong and partially coupled modes). The intensity profile of the source function is depicted in figure 2(c) and the intensity distributions resulting from this source at all three receiving planes are shown in figure 2(d).

Incorporating weakly coupled modes is impractical, as the improvement in reconstruction accuracy comes at the cost of an exponential increase in the source amplitudes [35]. Owing to the tunneling-like escape of waves, the field generated by such high-energy source functions remains largely confined

just outside the target planes, which results in inefficient reconstruction of the desired profiles. This behavior is illustrated in supplementary figure S3, in which the mean squared error (MSE) between the reconstructed and target profiles is evaluated to assess the reconstruction accuracy as a function of the number of modes included in the synthesis. When incorporating modes beyond the range of strongly coupled and partially coupled modes (usable modes), the energy distribution outside the target planes increases much more rapidly than the gains in reconstruction accuracy. For the configuration with $L = 0.125L_0$ in which the number of usable modes is smaller than the case with $L = 0.5L_0$, the reconstruction accuracy is analyzed as a function of the number of modes in supplementary figure S4.

Next, we structure arbitrary phase profiles in the receiving planes of the configuration in figure 2(b). As an example, we design two-dimensional (2D) phase-singularity sheets. In contrast to inverse design approaches which rely on maximizing the phase gradient at the desired singularity locations [47, 48], our method simply imposes target profiles with a π-phase discontinuity at those points. Here we assume the target phase profiles consisting of the digits '1', '2', and '3', defined with a phase of $\pi/2$ radians inside each digit's contour and $3\pi/2$ radians outside. The target amplitude is set to zero along each singularity contour and to a uniform unit value elsewhere (see supplementary figure S5). These zero-amplitude contours are not strictly required but are imposed to match the rigorous mathematical definition of dark intensity loci in phase singularity sheets. Figure 2(e) shows the projection of this target structure onto the receiving basis and the corresponding source field obtained from the first 357 well-coupled modes. The reconstructed phase and intensity (in dB) at the receiving planes are shown in figure 2(f). These fields represent the physically realizable wave emerging from the finite source aperture, with singular points reaching intensities as low as -24 dB across all planes. Approaching mathematically exact sheet singularities (with vanishing field amplitude) requires incorporating weakly coupled modes. Supplementary figure S6 shows the reconstructed profiles when the first 500 modes are incorporated, for which the minimum intensity at the singular points decreases to -41 dB.

3. Experimental setup

Several structured wave patterns were generated at $\lambda = 532$ nm using a phase-only reflective SLM with an 8 μm pixel pitch. The source function could not be directly encoded onto the SLM because it contains non-radiative (reactive) near-field components with transverse spatial frequencies exceeding the free-space propagation limit, and thus cannot be realized using a planar unitary phase modulator (see supplementary figure S7). These components correspond to near-zone terms of the Green's function which arise due to the finite extent of the source and receiving planes. Additionally, the source function exhibits large amplitude values associated with diffraction orders, arising from the discrete sampling grid ($d_x = d_y > \lambda$), which are incompatible with the finite phase quantization of the SLM (10-bit resolution, 1024 phase levels). For these reasons, we instead encode the field propagated from the source plane to $z = L_0$. At this distance, the field contains only propagating components, with all evanescent contributions exponentially suppressed. Moreover, higher diffraction orders are spatially separated at $z = L_0$ and lie entirely outside the source aperture size, so that only the zeroth order is encoded; see, e.g. the dashed white square in figure 3(b).

To realize a complex field profile using a phase-only mask, several hologram generation algorithms have been proposed, with their performance typically evaluated in terms of reconstruction quality and diffraction efficiency [50]. These methods rely on phase gratings to separate the shaped field—usually encoded in the first diffraction order—from the unshaped component. Here, we employ the algorithm of [49] (CGH of Type 3), which provides high-fidelity recovery of the encoded complex field compared to other hologram generation algorithms, as reported in [50]. This algorithm fixes the modulation depth of the CGHs to only 1.17π, see figure 3(c). As a consequence, it yields relatively low diffraction efficiency, reducing the intensity of the first-order diffracted field.

The experimental setup is depicted in figure 3(d). Before the SLM, the incident laser beam is collimated and expanded to illuminate the utilized SLM display area as a uniform quasi plane wave. A 4*f* imaging system is placed after the SLM to reconstruct the encoded complex field. At the Fourier plane an iris is placed to spatially filter the first diffraction order. The wave solution is projected at the front focal length of the second lens. In the encoding algorithm, the wave solution is interpolated to the utilized SLM display resolution (801×801 pixels), resulting in a SLM magnification of $M_{\mathrm{SLM}} = 800 \times 8\mu/Y_s \approx 12.03$. To produce a continuous light wavefront, the SLM pixel pitch δ must

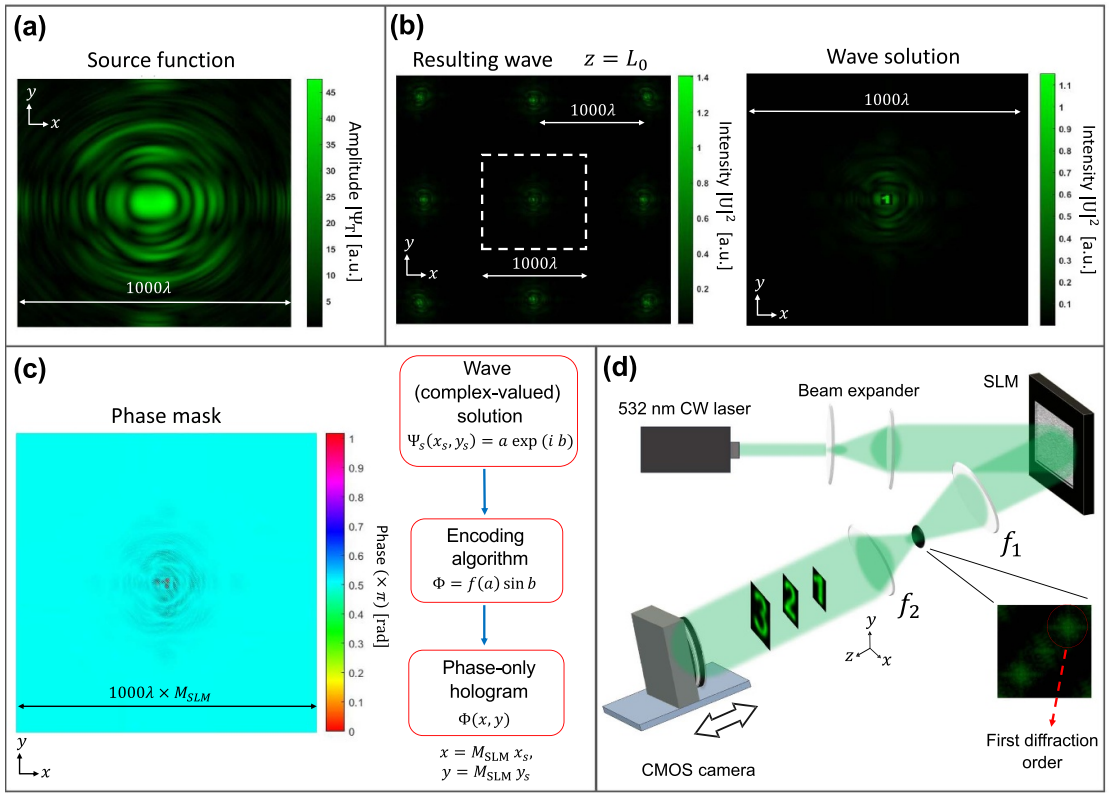

Figure 3. Optical reconstruction of the light waves using a phase-only reflective SLM. (a) Reactive near-field components and their strong diffraction-order amplitudes prevent direct encoding of the source function into a phase-only CGH. (b) The wave solution propagated from the source function to the plane $z = L_0$ was encoded instead as this Fresnel field is fully radiative and with no contributions from higher diffraction orders. The dashed white square highlights the aperture size. (c) The wave solution is interpolated to the utilized SLM display resolution (801 × 801 pixels) and is converted into a phase mask using the deterministic hologram generation algorithm of [49]. The algorithm encodes the wave solution on the first diffraction order of the phase mask in the spatial frequency domain. (d) Optical setup: a green laser is expanded and collimated before impinging on the SLM. After the SLM, a 4*f* system is employed to recover the wave solution at the front focal plane of the second lens. An iris is placed at the Fourier plane to filter the first diffraction order while blocking the SLM unmodulated wave (zeroth diffraction order). The intensity distributions of the resulting wave are recorded using a CMOS camera mounted on a translational stage. The phase profiles are reconstructed using the method of single-beam multiple-intensity reconstruction. Adapted with permission from [40] © 2025 Optica Publishing Group

satisfy the criterion of equation (10) with the input transverse (X_S and X_n) and longitudinal (z_n) dimensions scaled up by $\times M_{\mathrm{SLM}}$ and $\times M_{\mathrm{SLM}}^2$, respectively. For the configuration of figure 2(b), the criterion yields $\delta < 65.44\lambda$, which is fulfilled for our employed SLM with pixel pitch $\delta = 8\,\mu\mathrm{m} \approx 15.03\lambda$.

To obtain a light field with the same transverse dimensions and longitudinal separations as those of the receiving planes in the configuration of figure 2(b), the aspect ratio of the 4*f* system must compensate for the SLM magnification M_{SLM}. This requires $M_{4f} = f_2/f_1 = 1/M_{\mathrm{SLM}} \approx 1/12.03$. However, to facilitate the measurements, we adopted $f_2/f_1 = 2/3$, which results in an $\times 8.02$ magnification for the transverse dimensions and a stretching of $\times 8.02^2 = \times 64.32$ in the longitudinal separation distances between the target planes. The propagated fields from the implemented CGHs were recorded using a CMOS camera mounted on a translation stage as illustrated in figure 3(d). The phase profiles were retrieved using the single-beam multiple-intensity reconstruction (SBMIR) method [51], in which the complex field at the plane of interest is reconstructed from a series of intensity measurements taken at multiple planes along the propagation direction without the use of a reference beam. For details, see supplementary note 2. In our case, holographic interference methods could not provide the same robustness as the SBMIR method since the reference beam cannot maintain optimal interference simultaneously in all the planes, which would lead to non-uniform phase sensitivity.

Table 2. Quantitative metrics for experimentally reconstructed intensity profiles in figure 4(a).

Plane	MSE	SBR	Speckle Contrast C
1	0.0452	11.68	0.139
2	0.0729	9.31	0.231
3	0.1006	5.70	0.357

Table 3. Quantitative metrics for experimentally reconstructed phase profiles in figure 4(c).

Plane	MSE	$\sigma_{\text{int}}(\times\pi)$	$\sigma_{\text{out}}(\times\pi)$
1	0.0712	0.1616	0.0708
2	0.1172	0.1449	0.1153
3	0.1924	0.4667	0.2953

4. Results

We first experimentally reconstruct the multi-plane intensity-only case of figure 2(d). The measured intensity and retrieved phase distributions at the three target planes are shown in figures 4(a) and (b). To quantify the fidelity of the reconstructed profiles, we evaluated the MSE, signal-to-background ratio (SBR) and speckle contrast (C) as defined in Methods. Table 2 summarizes these results. Across all planes, the measured intensity profiles closely match the target patterns with MSE $\leqslant 0.1$. The SBR exceeds 5.5 in every plane, indicating strong suppression of inter-plane crosstalk and the absence of visible ghosting artifacts. In addition, speckle contrast remains relatively low, confirming that the deterministic superposition of communication modes yields locally smooth intensity profiles. Although no explicit phase constraints are imposed in the intensity-only reconstructions, the recovered complex fields exhibit smooth and physically consistent phase distributions—see figure 4(b) — across all planes. Instead of exhibiting arbitrary or uncorrelated phase patterns, the reconstructed fields correspond to a single global solution of the scalar wave equation imposed by the superposition of the communication modes.

We next experimentally demonstrate the synthesis of 2D phase-singularity sheets across multiple planes. Figures 4(c) and (d) present the measured phase distributions and intensity (in dB) for the example of figure 2(f), showing that the prescribed zero-amplitude contours coincide with sharp π phase transitions, forming continuous phase-singularity sheets that persist across all target planes. Quantitative phase reconstruction metrics are reported in table 3. The MSE of the phase profiles remains low across all planes, indicating a high global phase fidelity. Furthermore, the standard deviation within the interior of each digit region (σ_{int}) and the outside region (σ_{out}) confirms good local phase uniformity away from the singularity contours. The measured minimum intensity at the singular points reaches values below -24 dB—see figure 4(d), demonstrating the formation of physically realizable phase-singularity sheets with strong intensity suppression at the prescribed locations.

Now we apply the proposed method to the synthesis of higher-resolution patterns containing more stringent constraints in each target plane. As predicted by equation (8), the number of strong modes supported at each receiving plane increases with the array size of the receiving planes. Figure 5(a) shows two receiving planes, each consisting of a 41×41 array of receiving points, supporting $N = 400$ strong modes per plane. Achieving this higher spatial resolution—while preserving the source aperture size from figure 1(a) and ensuring $N = 400$ strongly coupled modes—imposes a constraint on the allowable separation between the target planes. The number of strong modes starts to decrease for separations smaller than $L = 0.25L_0$ (see supplementary figure S8). At a separation distance of $L = L_0$, a checkerboard pattern is structured at the first receiving plane, while a pattern composed of the binary digits '123' is projected at the second plane. Figures 5(b) and (c) show the projection of these target profiles onto the receiving basis, displayed as intensity and phase distributions using the same target values as in figure 2. The corresponding source functions (insets) are computed using the first 912 well-coupled modes, which accounts for all strong and partially coupled modes. Figures 5(d) and (e) present the simulated wave fields at the receiving planes and the experimentally measured intensity and phase profiles using the SLM optical setup of figure 3, for both target profiles. Quantitative metrics for these measured profiles are presented in table S2. Although a moderate increase in reconstruction error is observed relative to figure 4, the experimentally reconstructed intensity and phase profiles remain in good qualitative agreement with the designed targets across all planes, with the main structural features preserved.

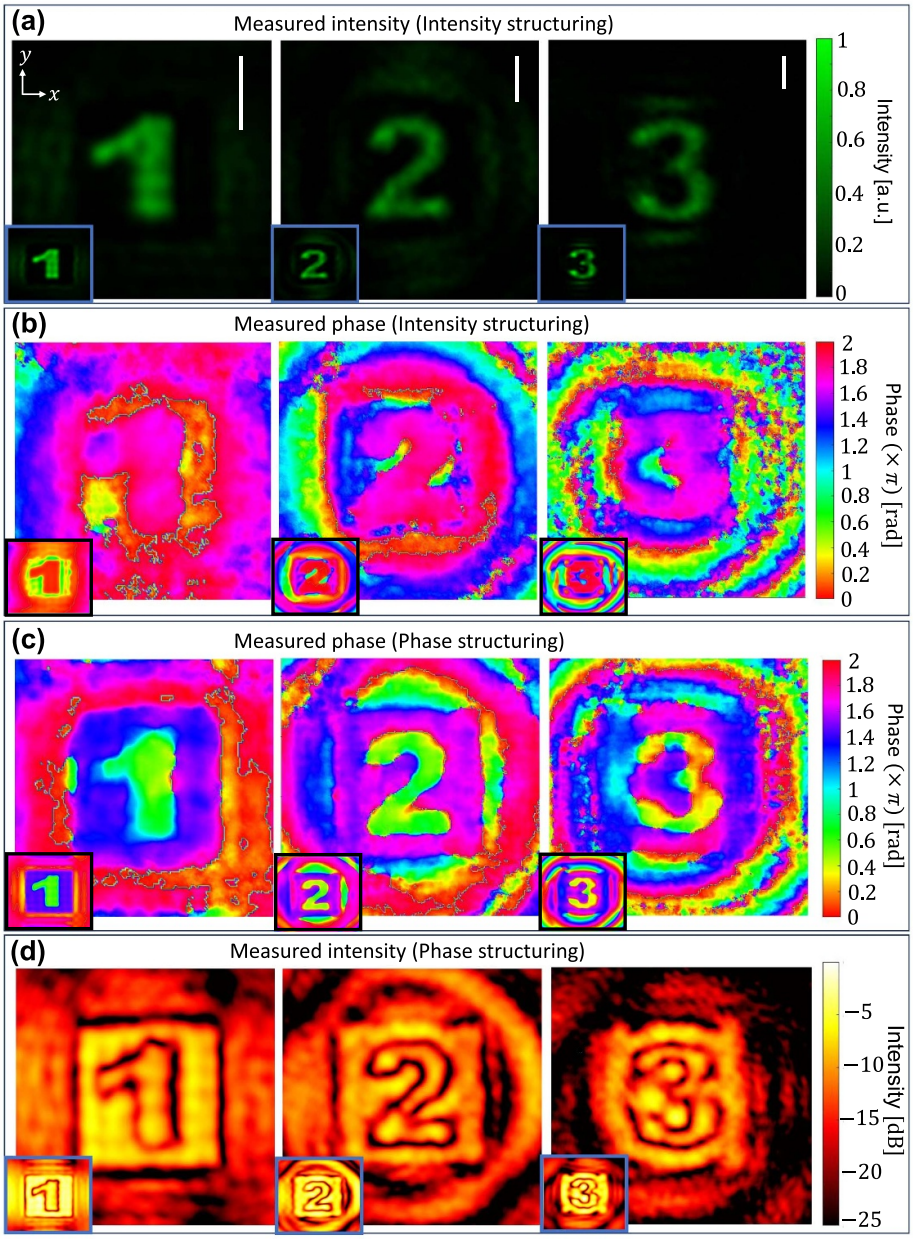

Figure 4. Optical reconstruction of the light waves using a phase-only reflective SLM. (a) Measured intensity and (b) retrieved phase distributions for the intensity-only target patterns of figure 2(d) at the three receiving planes. The reconstructed intensity profiles exhibit high fidelity, high contrast, and low speckle noise. (c) Measured retrieved phase and (d) intensity distributions for the target patterns of the example of figure 2(f). The digit contours correspond to zero-amplitude lines where phase jumps of π are imposed, forming two-dimensional phase-singularity sheets across all planes. Quantitative reconstruction metrics are reported in tables 2 and 3. Scale bars (vertical white lines) represent 0.1 mm. The second and third planes are longitudinally spaced by 68.4 mm and 136.8 mm from the first plane. Inset figures show the simulated intensity and phase distributions.

Additionally, the reconstructed phase distributions maintain coherent phase structure and sharp transitions at prescribed intensity minima, confirming that physically consistent complex-field solutions are enforced even in this more demanding scenario.

Since the communication modes are inherently complex-valued eigenfunctions, the proposed framework enables direct and simultaneous control of both amplitude and phase across all target planes as a unified complex field. Unlike conventional multi-plane holography, where amplitude constraints are enforced independently at each plane and phase is either unconstrained or indirectly optimized, our approach constructs a single physically consistent wavefront that satisfies all amplitude and phase requirements (imposed as target profiles) simultaneously, without iterative refinement. As an example, figure 6 shows simulated and measured results for target intensity patterns—the same digits from figure 2(b) — combined with a vortex phase profile $\exp(i\phi)$, demonstrating pixel-level control of both intensity and phase.

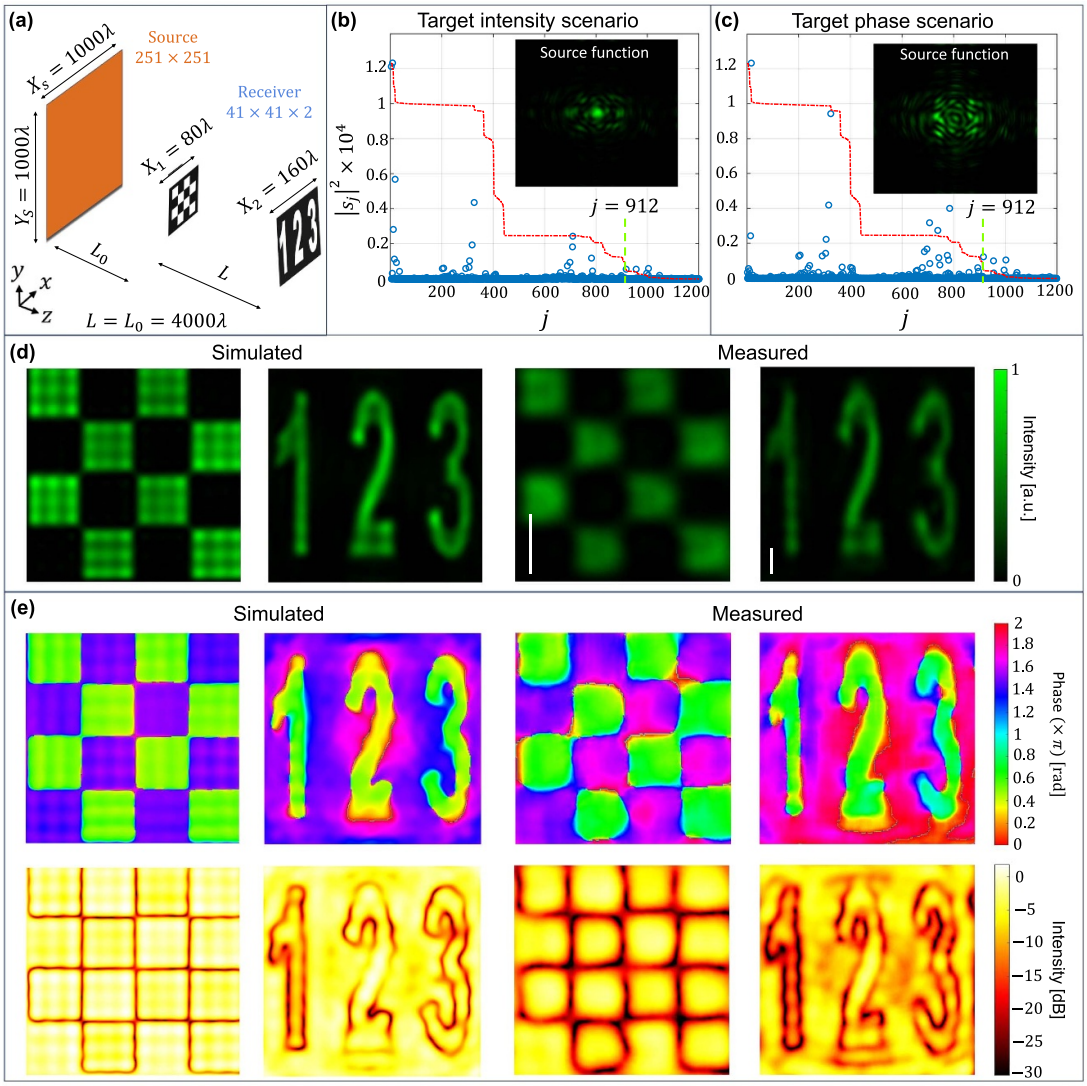

Figure 5. Structuring high-resolution and multi-plane complex amplitude wavefront profiles. (a) The number of supported strong modes in each receiving plane is increased by the array size. The same configuration of figure 1(a) with $L = L_0$ and receiving planes composed of 41 × 41 receiving points, resulting in 400 strong modes in each plane. (b) Projection of the target patterns (checkerboard and sequence of digits '123') as intensity profiles and (c) as phase profiles. The inset figure shows the required source function computed from the first 912 well-coupled modes. Simulated resulting wave at the receiving planes and measured reconstructed profiles when the target patterns are (d) intensity-only profiles and (e) phase profiles (with the same target values as in figure 2). Scale bars (vertical white lines) represent 0.1 mm. The measured planes are longitudinally spaced by 136.8 mm.

Additional experimental results illustrating the robustness of the proposed framework are presented in supplementary figure S9. These measurements correspond to a configuration of three target planes in the non-paraxial regime as shown in figure S9(a). The same target phase profiles as in figure 2 are assumed and the source function is synthesized from the first 250 well-coupled modes—see figure S9(b). Measured retrieved phase profiles are presented in figure S9(c) and these distributions remain in good agreement with the designed targets (MSE values shown in white). In the non-paraxial regime, the number of strongly coupled modes increases with propagation and reaches the heuristic value (equation (7)) only near the paraxial regime; nevertheless, the field structure remains qualitatively intact and inter-plane crosstalk is strongly suppressed. These results confirm that the proposed approach provides a stable and predictable route to multi-plane field synthesis for distinct configurations of target planes.

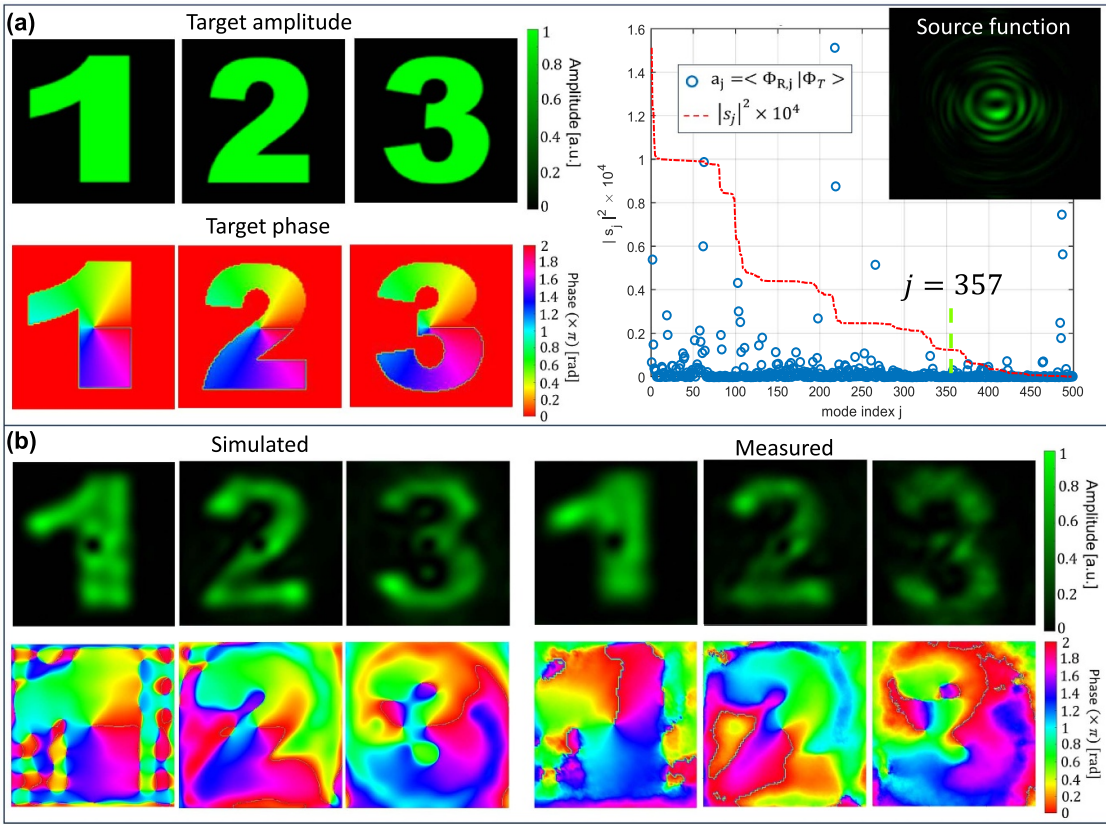

Figure 6. Simultaneous modulation of amplitude and phase. (a) Target distributions consisting of prescribed intensity patterns (digits '1', '2', and '3') combined with a vortex phase profile of the form $\exp(i\phi)$. The projection onto the receiving basis and the corresponding source function (inset) are computed using the communication modes framework. (b) Simulated and experimentally measured reconstructed intensity and phase distributions at the target planes. The results demonstrate pixel-level control of complex-valued fields and the ability to encode structured phase profiles on top of arbitrary intensity patterns within a single physically consistent wavefront.

5. Conclusions

We introduced and experimentally demonstrated a deterministic framework for 3D beam shaping that enables versatile control of intensity and phase across multiple axial planes. By expressing target fields as a linear superposition of free-space communication modes obtained from the SVD of a source–receiver coupling operator, the proposed approach constructs a single physically consistent wavefront rather than a set of independently reconstructed planes. Unlike iterative and inverse-design holographic techniques, which suppress inter-plane crosstalk by randomizing phase and thereby relinquish deterministic phase control, our method enforces phase coherence across planes by construction. This enables speckle-free reconstruction of intensity profiles. The method also enables the generation of arbitrary phase profiles, including continuous topological features such as 2D phase-singularity sheets, as a unified solution of the wave equation that satisfies all plane constraints simultaneously, rather than as separate, unrelated phase patterns. As illustrated in supplementary video 2, the reconstructed intensity and phase profiles evolve smoothly along the propagation direction for the example in figure 4(c).

Computing the communication modes requires an SVD of the coupling matrix G_{SR}, with cost approximately $\mathcal{O}(N^2)$ in the number of strongly coupled modes N supported by each target plane for a given source aperture (see supplementary figure S10). This operation is performed once for a fixed geometry and wavelength, after which arbitrary target fields are deterministically synthesized without iterative optimization. By contrast, standard multi-plane holographic techniques recover the source function via iterative forward–backward propagation with alternating amplitude and phase constraints, requiring repeated execution for each target distribution and exhibiting sensitivity to initialization, convergence pathways and noise accumulation in a non-convex optimization problem. In supplementary figure S11, the GGS algorithm, as implemented in [12], is applied to the configuration of figure 2(b)

for the reconstruction case of figure 2(d). The source function is initialized with a random phase distribution and the Green's function operator kernel (equation (2)) is used as a propagation model. The algorithm stagnates after about 200 iterations (with relative change in reconstruction $\Delta < 10^{-6}$), yielding reconstructions that remain less accurate than those of the proposed method, as quantified by MSE and structural similarity index measure (SSIM) metrics (figure S11). Our formulation avoids cumulative noise effects and yields inherently more robust solutions. Experimentally, robustness is assessed by the consistent low MSE values as reported in tables 2, 3 and S3. Additionally, the frame-to-frame intensity fluctuations at the same measurement plane remain below 6.6% of the maximum intensity across all configurations, confirming the stability of the experimental results (see $\sigma_{\max}/I_{\max}$ in table S2).

Beyond providing high fidelity reconstructions, the presented framework clarifies the physical limits of volumetric wave shaping with finite apertures. The communication modes define the complete set of volumetric fields that can be transmitted with high efficiency, revealing if certain field structures can be physically constructed or not based on the coupling strength of these modes. In this sense, SVD modal optics establishes a physically grounded basis for understanding and designing volumetric wave fields. In particular, inter-plane crosstalk is automatically eliminated through the linear superposition of the communication modes. Among these modes, the extrinsic ones—those imposed on each receiving plane by the presence of the other receiving planes—play a key role in suppressing coherent traces of adjacent-plane reconstructions. This effect is analyzed in supplementary figure S12, where we show that excluding the extrinsic modes for the configuration in figure 2(b) leads to degraded reconstruction of the target intensity profiles. In this case, measured profiles yield MSE > 0.1 and SBR < 4.2 in each plane. Furthermore, diffraction limits can be straightforwardly identified by computing the singular values for a given configuration of receiving planes and aperture size (i.e. a given coupling matrix G_{SR}) and comparing the number of strongly coupled modes with the total number of designed modes. This analysis reveals a minimum separation distance L between planes: reducing L below this threshold requires incorporating a substantial number of weakly coupled modes, which in turn demands excessively large source amplitude functions that are impractical to implement. Because the weak coupling strengths exhibit a universal rapid fall-off [45], these limits are also universal; consequently, no other wave-shaping technique can yield physically realizable solutions in this sub-diffraction regime.

Deterministic control of phase enables a broad class of applications, including depth-dependent aberration correction, multi-plane structured illumination, and volumetric optical trapping based on phase-gradient forces. Beyond these examples, the proposed framework may extend to volumetric optical computing and diffractive neural networks, where programmable 3D operators require independent phase control per plane with reduced interlayer crosstalk. Multi-plane phase control further enables the engineering of constructive and destructive interference throughout the propagation volume, a capability central to nonlinear optical processes and quantum control schemes that rely on phase matching and coherent interaction across depths. More generally, the present results establish that SVD modal optics provides a physically consistent framework for multi-plane beam shaping in regimes where phase structure and coherence are important design considerations.

6. Methods

6.1. Communication modes optics

We assume the source and receiving spaces described respectively by vector positions $\mathbf{r}_S$ and $\mathbf{r}_R$. For a given operating wavelength λ in free-space and time harmonic dependence $\exp(-\mathrm{i}\omega_0 t)$ with $\omega_0 = kc$ and $k = 2\pi/\lambda$, the propagation of a continuous resulting wave $U(\mathbf{r}_R)$ created by a spatially continuous source function $\Psi_S(\mathbf{r}_S)$ is governed by the Helmholtz equation $\nabla^2 U(\mathbf{r}_R) + k^2 U(\mathbf{r}_R) = \Psi_S$. Its solution for a linear medium is the integral equation $U(\mathbf{r}_R) = \int_{V_s} G_{SR,\lambda}(\mathbf{r}_R, \mathbf{r}_S)\Psi_S(\mathbf{r}_S)\mathrm{d}^3(\mathbf{r}_S)$, computed at the source volume V_s, and G_{SR} being the usual free-space scalar Green's function [52]:

$$G_{SR,\lambda}(\mathbf{r}_R, \mathbf{r}_S) = -\frac{1}{4\pi}\frac{\exp(\mathrm{i}k|\mathbf{r}_R - \mathbf{r}_S|)}{|\mathbf{r}_R - \mathbf{r}_S|}, \tag{1}$$

and the boundary conditions are those of an open, unbounded free-space medium with no reflections.

To describe G_{SR} in a matrix form, we assume the source space as a collection of N_S source points located at positions $\mathbf{r}_{S,j}$ $(j = 1, \ldots, N_S)$. Similarly, the receiving space is a collection of N_R receiving points at positions $\mathbf{r}_{R,i}$ $(i = 1, \ldots, N_R)$. With this description, each source and receiving eigenfunction, $|\Psi_S\rangle$ and

$|\Phi_R\rangle$, is mathematically a column vector, whose elements are complex-valued amplitudes at each different point in the appropriate space. This results in a $N_R \times N_S$ matrix for G_{SR}:

$$g_{ij} = -\frac{1}{4\pi}\frac{\exp\left(ik|\mathbf{r}_{R,i} - \mathbf{r}_{S,j}|\right)}{|\mathbf{r}_{R,i} - \mathbf{r}_{S,j}|}. \tag{2}$$

The concept of communication modes is established by the following two eigen-equations [35–37]:

$$G_{SR}^{\dagger} G_{SR} \left|\Psi_{S,j}\right\rangle = |s_j|^2 \left|\Psi_{S,j}\right\rangle, \tag{3a}$$

$$G_{SR} G_{SR}^{\dagger} \left|\Phi_{R,j}\right\rangle = |s_j|^2 \left|\Phi_{R,j}\right\rangle, \tag{3b}$$

in which $G_{SR}^{\dagger} G_{SR}$ is a $N_S \times N_S$ matrix, i.e. an operator within the source space. Similarly, $G_{SR} G_{SR}^{\dagger}$, with size $N_R \times N_R$, is an operator within the receiving space. Both are Hermitian and positive operators, implying that their eigenvalues are real positive numbers and that their eigenfunctions are orthogonal and form complete sets for the spaces. Additionally, the eigenvalues $|s_j|^2$, known as coupling strengths, correspond to the squared amplitude of the singular values s_j of G_{SR}. In fact, from the two eigen-equations in equation (3) we obtain the following one-to-one relationship between the source and receiving eigenfunctions:

$$G_{SR} \left|\Psi_{S,j}\right\rangle = s_j \left|\Phi_{R,j}\right\rangle. \tag{4}$$

The relation in equation (4) defines the concept of a communication mode: a pair of eigenfunctions, one at the source space $\left|\Psi_{S,j}\right\rangle$ and one at the receiving space $\left|\Phi_{R,j}\right\rangle$, with the strength of this connection established by the coupling strength $|s_j|^2$. Each source eigenfunction $\left|\Psi_{S,j}\right\rangle$ creates a resulting wave in the receiving space that has the form of the receiving eigenfunction $\left|\Phi_{R,j}\right\rangle$ weighted by the complex amplitude s_j. Another property from the operators $G_{SR}^{\dagger} G_{SR}$ and $G_{SR} G_{SR}^{\dagger}$ is that their eigenfunctions and eigenvalues satisfy maximization properties, i.e. each successive receiving eigenfunction $\left|\Phi_{R,j}\right\rangle$ corresponds to the next largest possible magnitude of wave function its associated source eigenfunction $\left|\Psi_{S,j}\right\rangle$ can create at the receiving space [35].

6.2. Design of the source and receiving planes

The spacing distances $d_{x,n}$ and $d_{y,n}$ in each receiving nth plane must be designed based on the minimum spot length that can be structured from the source aperture along each transverse direction. In the paraxial regime, these quantities depend on the distance from the aperture $z_n = L_0 + (n-1)L$ as well as the aperture size (X_s and Y_s) [53]:

$$\delta_{x,n} = \frac{\lambda z_n}{X_s} \quad ; \quad \delta_{y,n} = \frac{\lambda z_n}{Y_s}. \tag{5}$$

Setting the spacing distances $d_{x,n}$ and $d_{y,n}$ to satisfy the sampling rate according to the Nyquist theorem, i.e. $d_{x,n} = \delta_{x,n}/2$ and $d_{y,n} = \delta_{y,n}/2$, leads to:

$$d_{x,n} = \frac{\lambda}{2}\frac{z_n}{X_s} \quad ; \quad d_{y,n} = \frac{\lambda}{2}\frac{z_n}{Y_s}, \tag{6}$$

which implies a linear growth of the transverse dimensions of the receiving planes, $X_n = (p_{x,r,n} - 1)d_{x,n}$ and $Y_n = (p_{y,r,n} - 1)d_{y,n}$, with the distance from the source plane, in accordance with diffraction from a planar aperture [1]. The pyramidal volume defined by these dimensions represents the alias-free propagation region for an aperture sampled on a rectangular grid with spacing $d_x = d_y > \lambda$ [53].

Now we evaluate the number of strong modes that each receiving plane can support using the paraxial heuristic number as defined in [35, 37] between a source plane and a single receiving transverse plane. This number corresponds to the maximum number of intensity fringes that can be formed in the receiving plane:

$$N_{H,n} = \frac{X_s X_n}{\lambda z_n}\frac{Y_s Y_n}{\lambda z_n}. \tag{7}$$

In the paraxial regime, the 'Nyquist' heuristic counting, as given by equation (7), corresponds to the point at which the singular values from the communication modes analysis begin to fall off quasi-exponentially [35]. Beyond the paraxial approximation, this simple heuristic number no longer applies,

although the full communication modes analysis can still be used to determine the usable modes. Substituting the relations in equation (6) into equation (7), results in:

$$N_{H,n} = (1/4)\left(p_{x,r,n} - 1\right)\left(p_{y,r,n} - 1\right), \tag{8}$$

i.e. it corresponds to the number of points in the receiving array plane, so we are only using as many sampling points as we need for the number of strongly coupled modes. Incorporating more sampling points while keeping the dimensions of the receiving planes fixed does not increase the number N of supported strong modes per plane. Setting the same number of receiving points for all the n planes, i.e. $p_{x,r,n} = p_{y,r,n} = p_r$, all of them support the same number of strong modes. From the relations in equation (6) and using that $X_s = Y_s = 4L_0$, the spacing distances are written in terms of (L_0/L) and n as:

$$d_{x,n} = d_{y,n} = 2\lambda\left[1 + (n-1)\frac{L}{L_0}\right]. \tag{9}$$

Therefore, we first specify the source dimensions, X_s and Y_s, and determine the transverse spacing distances in the receiving planes according to equation (9) for a given value for the ratio L/L_0. In all our examples in the main manuscript, we assumed $X_s = Y_s$ and $L_0 = 4Y_s$. Finally, the spacing distances in the source plane, $d_x = d_y$, are chosen such that the resulting wave created by the N_s source points is essentially the same as if it had a continuous source. In other words, we need to guarantee that the wave created by each source point is the same as a patch with the source point amplitude uniformly distributed over the area $d_x d_y$. To do this, we follow the procedure done in [40]. First, for the largest distance between the source plane and each receiving plane, we compute the phase difference between the waves created by a point at the middle of the patch and one at the end of the patch (lying on the diagonal of the patch). Since destructive interference between these waves starts to occur if this phase difference is larger than $\lambda/2$, we then establish a criterion for the source spacings by setting this phase difference to be less than $\lambda/2$:

$$d_x = d_y < \frac{\lambda}{\sqrt{2}}\frac{\sqrt{(X_s + X_n)^2/2 + z_n^2}}{(X_s + X_n)/2}, \tag{10}$$

for each receiving plane n. The criterion of equation (10) is applied for $n = 1$ since the first receiving plane imposes the smallest value for d_x.

6.3. Synthesis of light waves based on communication modes

The required source function to create a target complex-valued profile in the receiving space is [2, 35]:

$$|\Psi_T\rangle = \sum_j \frac{1}{s_j}\langle\Phi_{R,j}|\Phi_T\rangle\left|\Psi_{S,j}\right\rangle, \tag{11}$$

in which $\langle\Phi_{R,j}|\Phi_T\rangle$ is the projection of the target profile onto the set of receiving eigenfunctions.

The resulting wave created by this source function at a position $\mathbf{r}$ from the source plane is given by summing up the spherical waves emitted by the N_s source points weighted by $|\Psi_T\rangle$ [35]:

$$U(\mathbf{r}) = -\frac{1}{4\pi}\sum_{q=1}^{N_S}\frac{\exp\left(ik|\mathbf{r} - \mathbf{r}_{S,q}|\right)}{|\mathbf{r} - \mathbf{r}_{S,q}|}h_q, \tag{12}$$

where h_q is the qth component of the source function $|\Psi_T\rangle$ on the source basis $\{\left|\Psi_{S,j}\right\rangle\}$.

6.4. Reconstruction quality metrics

MSE:

$$\mathrm{MSE} = \frac{1}{N}\sum_{i=1}^{N}\left[f_{\mathrm{meas}}(i) - f_{\mathrm{targ}}(i)\right]^2, \tag{13}$$

where the summation is taken over the N pixels of the CMOS camera within the target plane. All intensity distributions were normalized to their respective maximum values within each plane prior to computing MSE. Similarly, for phase reconstructions, the phase ϕ was first normalized as $(\phi - 0.5)/\pi$.

SBR:

$$\mathrm{SBR} = \frac{< I_{\mathrm{sig}} >}{< I_{\mathrm{bg}} >}, \tag{14}$$

where $< I_{sig} >$ denotes the mean intensity within regions corresponding to the target signal (bright regions), and $< I_{bg} >$ is the mean intensity within nominally dark background regions. The signal and background regions were defined based on the target intensity distribution using a fixed intensity threshold of 50% of the maximum intensity.

Speckle contrast: Local intensity fluctuations within nominally uniform bright regions were characterized using speckle contrast:

$$C = \frac{\sigma_I}{< I >}, \tag{15}$$

in which σ_I and $< I >$ are the standard deviation and mean of the intensity evaluated over the signal regions. Edge regions were excluded by morphological erosion to avoid bias from intensity gradients.

6.5. Experimental setup

As a light source, an Oxxius L1C+-532S 532.3 nm diode pumped solid state laser was used in conjunction with a pinhole spatial filter setup (horizontal polarization ensured by $\lambda/2$-plate and Thorlabs LPVIS050-MP2 polarizer, 30μm pinhole, 20x objective, 750 mm collimating plano-convex lens) to generate a well collimated Gaussian beam of sufficient diameter. Collimation was confirmed using a Thorlabs WFS20 Shack-Hartman Wavefront sensor. The radius of curvature was over 100 m.

The CGHs were generated using a Santec SLM-200 at normal incidence combined with a 4*f* system of magnification $M_{4f} = 100/150 = 2/3$ for Fourier-order filtering, employing plano-convex lenses. A non-polarizing cube-beam-splitter was used to couple the SLM output into the 4*f* Fourier filter, where a diffraction order was chosen using an iris. Longitudinal distance between the 4*f* lenses was also optimized to a radius of curvature over 50 m with an incident flat wavefront. The second lens of the 4*f* Fourier filter was shifted laterally to accommodate the chosen Fourier order.

Intensities of the CGHs were measured using a monochromatic IDS U3-3880CP-M-GL Rev.2.2 CMOS camera (2.4 μm pixel size) mounted on a Thorlabs LTS150C/M linear stage. The total magnification of the system, product of the 4*f* magnification and the SLM magnification due to rescaling compared to the SVD design geometry, $M_{SLM}M_{4f}$, was chosen to fit the 150 mm of stage travel, so the full 3D space of interest could be measured at once.

Acknowledgments

V.S.A. acknowledges financial support from the Coordination of Superior Level Staff Improvement (CAPES), Grant No. 88887.833874/2023-00, and from the National Council for Scientific and Technological Development (CNPq), Grant No. 140270/2022-1. A.H.D. acknowledges financial support from the Dutch Research Council (NWO) under the Vidi program (Grant No. VI.Vidi.243.137) and from the Optica Foundation. L.A.A. acknowledges financial support from the National Council for Scientific and Technological Development (CNPq), Grant No. 309201/2021-7, and from the São Paulo Research Foundation (FAPESP), Grant No. 2025/28712-1. F.C. acknowledges financial support from the Office of Naval Research (ONR) under the MURI programme, Grant No. N00014-20-1-2450, and from the Air Force Office of Scientific Research (AFOSR) under Grant Nos. FA9550-21-1-0312 and FA9550-22-1-0243. D.A.B.M. also acknowledges support from AFOSR Grant FA9550-21-1-0312.

Data availability statement

The data that support the findings of this study are openly available at the following URL/DOI: https://doi.org/10.6084/m9.figshare.32086752 [54]. Additional data sets and raw measurements are available from the corresponding author upon reasonable request.

Supplementary data 1 available at https://doi.org/10.1088/2040-8986/ae709d/data1.

Supplementary data 2 available at https://doi.org/10.1088/2040-8986/ae709d/data2.

Supplementary data 3 available at https://doi.org/10.1088/2040-8986/ae709d/data3.

Conflict of interests

The authors declare no competing interests.

Code availability

The code that supports the findings of this study are available online in the Figshare database under accession code https://doi.org/10.6084/m9.figshare.32086752.

Author contributions

Vinicius S de Angelis 0000-0002-4684-1134
Conceptualization (lead), Formal analysis (equal), Investigation (equal), Methodology (lead), Software (lead), Validation (equal), Visualization (equal), Writing – original draft (lead), Writing – review & editing (equal)

Maximilian Jeindl 0009-0006-1661-6629
Data curation (lead), Formal analysis (equal), Investigation (equal), Validation (equal), Writing – review & editing (equal)

Leonardo A Ambrosio 0000-0003-0404-9509
Validation (equal), Visualization (equal), Writing – review & editing (equal)

David A B Miller 0000-0002-3633-7479
Formal analysis (equal), Validation (equal), Visualization (equal), Writing – review & editing (equal), Investigation (supporting)

Federico Capasso 0000-0003-4534-8249
Validation (equal), Visualization (equal), Writing – review & editing (equal)

Ahmed H Dorrah 0000-0002-1643-0035
Formal analysis (equal), Investigation (equal), Project administration (lead), Resources (lead), Supervision (lead), Validation (equal), Visualization (equal), Writing – review & editing (equal), Conceptualization (supporting)

References

[1] Goodman J W 2005 *Introduction to Fourier Optics* (Roberts and Company)
[2] Piestun R and Shamir J 2002 Synthesis of three-dimensional light fields and applications *Proc. IEEE* **90** 222–44
[3] Grier D G 2003 A revolution in optical manipulation *Nature* **424** 810–6
[4] Blanche P-A 2021 Holography and the future of 3D display *Light: Adv. Manuf.* **2** 446
[5] Ginner L, Kumar A, Fechtig D, Wurster L M, Salas M, Pircher M and Leitgeb R A 2017 Noniterative digital aberration correction for cellular resolution retinal optical coherence tomography in vivo *Optica* **4** 924–31
[6] Lin X, Rivenson Y, Yardimci N T, Veli M, Luo Y, Jarrahi M and Ozcan A 2018 All-optical machine learning using diffractive deep neural networks *Science* **361** 1004–8
[7] Gerchberg R W and Saxton W O 1972 A practical algorithm for the determination of phase from image and diffraction plane pictures *Optik* **35** 237–46
[8] Fienup J R 1980 Iterative method applied to image reconstruction and to computer-generated holograms *Opt. Eng.* **19** 297–305
[9] Tricoles G 1987 Computer generated holograms: an historical review *Appl. Opt.* **26** 4351–60
[10] Ripoll O, Kettunen V and Herzig H P 2004 Review of iterative Fourier-transform algorithms for beam shaping applications *Opt. Eng.* **43** 2548–9
[11] Haist T, Schönleber M and Tiziani H 1997 Computer-generated holograms from 3D-objects written on twisted-nematic liquid crystal displays *Opt. Commun.* **140** 299–308
[12] Sinclair G, Leach J, Jordan P, Gibson G, Yao E, Laczik Z J, Padgett M J and Courtial J 2004 Interactive application in holographic optical tweezers of a multi-plane Gerchberg-Saxton algorithm for three-dimensional light shaping *Opt. Express* **12** 1665–70
[13] Zhang J, Pégard N, Zhong J, Adesnik H and Waller L 2017 3D computer-generated holography by non-convex optimization *Optica* **4** 1306–13
[14] Chen C, Lee B, Li N-N, Chae M, Wang Di, Wang Q-H and Lee B 2021 Multi-depth hologram generation using stochastic gradient descent algorithm with complex loss function *Opt. Express* **29** 15089–103
[15] Makey G, Yavuz O, Kesim D K, Turnalı A, Elahi P, Ilday S, Tokel O and Ilday F O 2019 Breaking crosstalk limits to dynamic holography using orthogonality of high-dimensional random vectors *Nat. Photon.* **13** 251–6
[16] Goodman J 2007 *Speckle Phenomena in Optics: Theory and Applications* (Roberts & Company)
[17] Aagedal H, Schmid M, Beth T, Teiwes S and Wyrowski F 1996 Theory of speckles in diffractive optics and its application to beam shaping *J. Mod. Opt.* **43** 1409–21
[18] Zhou P, Li Y, Liu S and Su Y 2019 Dynamic compensatory Gerchberg-Saxton algorithm for multiple-plane reconstruction in holographic displays *Opt. Express* **27** 8958–67
[19] Wang J, Wang J, Zhou J, Zhang Y and Wu Y 2023 Crosstalk-free for multi-plane holographic display using double-constraint stochastic gradient descent *Opt. Express* **31** 31142–57
[20] Senthilkumaran P, Wyrowski F and Schimmel H 2005 Vortex stagnation problem in iterative Fourier transform algorithms *Opt. Lasers Eng.* **43** 43–56

[21] Chang C, Bang K, Wetzstein G, Lee B and Gao L 2020 Toward the next-generation VR/AR optics: a review of holographic near-eye displays from a human-centric perspective *Optica* **7** 1563–78
[22] Li Y, Wu Y-L, Hoess P, Mund M and Ries J 2019 Depth-dependent PSF calibration and aberration correction for 3D single-molecule localization *Biomed. Opt. Express* **10** 2708–18
[23] Guo M *et al* 2025 Deep learning-based aberration compensation improves contrast and resolution in fluorescence microscopy *Nat. Commun.* **16** 313
[24] Berry M 2000 Making waves in physics *Nature* **403** 21–21
[25] Dennis M R, O'Holleran K and Padgett M J 2009 *Chapter 5 Singular Optics: Optical Vortices and Polarization Singularities* (Elsevier) pp 293–363
[26] Shen Y *et al* 2019 Optical vortices 30 years on: OAM manipulation from topological charge to multiple singularities *Light Sci. Appl.* **8** 90
[27] Xu P, He X, Wang J and Zhan M 2010 Trapping a single atom in a blue detuned optical bottle beam trap *Opt. Lett.* **35** 2164–6
[28] Yu H, Mao Z, Li J, Ye Y, Yin Y, Xia Y and Yin J 2020 Chip-scale molecule trapping by a blue-detuned metasurface hollow beam *J. Opt.* **22** 045104
[29] Barredo D, Lienhard V, Scholl P, de Léséleuc S, Boulier T, Browaeys A and Lahaye T 2020 Three-dimensional trapping of individual Rydberg atoms in ponderomotive bottle beam traps *Phys. Rev. Lett.* **124** 023201
[30] Huft P, Song Y, Graham T M, Jooya K, Deshpande S, Fang C, Kats M and Saffman M 2022 Simple, passive design for large optical trap arrays for single atoms *Phys. Rev. A* **105** 063111
[31] Piotrowicz M J, Lichtman M, Maller K, Li G, Zhang S, Isenhower L and Saffman M 2013 Two-dimensional lattice of blue-detuned atom traps using a projected Gaussian beam array *Phys. Rev. A* **88** 013420
[32] Ling C, Yin Y, Liu Y, Li L and Xia Y 2023 Generation of a blue-detuned optical storage ring by a metasurface and its application in optical trapping of cold molecules *Chin. Phys. B* **32** 023301
[33] Roichman Y, Sun B, Roichman Y, Amato-Grill J and Grier D G 2008 Optical forces arising from phase gradients *Phys. Rev. Lett.* **100** 013602
[34] Shi Y *et al* 2023 Advances in light transverse momenta and optical lateral forces *Adv. Opt. Photon.* **15** 835–906
[35] Miller D A B 2019 Waves, modes, communications and optics: a tutorial *Adv. Opt. Photon.* **11** 679–825
[36] Miller D A B 1998 Spatial channels for communicating with waves between volumes *Opt. Lett.* **23** 1645–7
[37] Miller D A B 2000 Communicating with waves between volumes: evaluating orthogonal spatial channels and limits on coupling strengths *Appl. Opt.* **39** 1681–99
[38] Thaning A, Martinsson P, Karelin M and Friberg A T 2003 Limits of diffractive optics by communication modes *J. Opt. A: Pure Appl. Opt.* **5** 153
[39] Burvall A, Martinsson P and Friberg A T 2004 Communication modes applied to axicons *Opt. Express* **12** 377–83
[40] de Angelis V S, Dorrah A H, Ambrosio L A, Miller D A B and Capasso F 2025 Structuring light waves in 3D volumes with high precision using communication mode optics *Optica* **12** 1502–13
[41] Shimobaba T and Ito T 2015 Random phase-free computer-generated hologram *Opt. Express* **23** 9549–54
[42] Nagahama Y, Shimobaba T, Kakue T, Takaki Y and Ito T 2019 Image quality improvement of random phase-free holograms by addressing the cause of ringing artifacts *Appl. Opt.* **58** 2146–51
[43] Chen L, Tian S, Zhang H, Cao L and Jin G 2021 Phase hologram optimization with bandwidth constraint strategy for speckle-free optical reconstruction *Opt. Express* **29** 11645–63
[44] Sui X, He Z, Chu D and Cao L 2024 Non-convex optimization for inverse problem solving in computer-generated holography *Light Sci. Appl.* **13** 158
[45] Miller D A B, Kuang Z and Miller O D 2025 Tunnelling escape of waves *Nat. Photon.* **19** 284–90
[46] Piestun R and Miller D A B 2000 Electromagnetic degrees of freedom of an optical system *J. Opt. Soc. Am. A* **17** 892–902
[47] Lim S W D, Park J-S, Meretska M L, Dorrah A H and Capasso F 2021 Engineering phase and polarization singularity sheets *Nat. Commun.* **12** 4190
[48] Lim S W D, Park J-S, Kazakov D, Spägele C M, Dorrah A H, Meretska M L and Capasso F 2023 Point singularity array with metasurfaces *Nat. Commun.* **14** 3237
[49] Arrizón V, Ruiz U, Carrada R and González L A 2007 Pixelated phase computer holograms for the accurate encoding of scalar complex fields *J. Opt. Soc. Am. A* **24** 3500–7
[50] Clark T W, Offer R F, Franke-Arnold S, Arnold A S and Radwell N 2016 Comparison of beam generation techniques using a phase only spatial light modulator *Opt. Express* **24** 6249–64
[51] Almoro P, Pedrini G and Osten W 2006 Complete wavefront reconstruction using sequential intensity measurements of a volume speckle field *Appl. Opt.* **45** 8596–605
[52] Hanson G and Yakovlev A 2001 *Operator Theory for Electromagnetics: An Introduction* (Springer)
[53] Piestun R, Spektor B and Shamir J 1996 Wave fields in three dimensions: analysis and synthesis *J. Opt. Soc. Am. A* **13** 1837–48
[54] de Angelis V S, Jeindl M, Ambrosio L A, Miller D A B, Capasso F and Dorrah A H 2026 Codes for Multi-plane spatially resolved phase structuring using optical communication modes *Figshare* (https://doi.org/10.6084/m9.figshare.32086752)